Edge-state-induced correlation effects in two-color pump-probe high-order harmonic generation

Simon Vendelbo Bylling Jensen,[1] Hossein Iravani,[2] and Lars Bojer Madsen[1]
[1]*Department of Physics and Astronomy, Aarhus University, DK-8000 Aarhus C, Denmark*
[2]*Department of Chemistry, Tarbiat Modares University, P.O. Box 14115-175, Tehran, Iran*

(Received 20 October 2020; revised 19 January 2021; accepted 5 May 2021; published 26 May 2021)

For a finite-sized generic nanostructured band gap material, it is shown that significant laser-induced correlation effects can be introduced by a two-color pump-probe scheme where edge states are resonantly pre-excited by the pump before the probe arrives and drives the generation of high-order harmonics. Compared with the response of a bulk sample, we demonstrate an increase in the efficiency of the generated high-harmonic signal over a wide range of frequencies by harnessing the power of these ultrafast many-electron dynamics.

DOI: 10.1103/PhysRevA.103.053121

I. INTRODUCTION

Since the demonstration of high-harmonic generation (HHG) in solids [1], the process has attracted increased interest due to its capability (i) to produce ultrafast coherent light pulses of high frequency [2–4] and (ii) to retrieve information about electron dynamics on an ultrafast timescale [5]. The mechanism responsible, although still being debated [6–17], is typically explained through a combination of intraband [1,10] and interband transitions [18]. The physics of the interband transitions has basic similarities with the three-step model of HHG in atoms [19–21]. Most of the theoretical frameworks [1–4,10–18] describing the behavior of HHG in solids are based on a static band structure picture, and HHG has also been used to reconstruct band structures [22]. Such an independent-electron approach may be justified when the beyond-mean-field electron-electron interaction is of minor importance for the initial state *as well as* for the HHG process. In typical semiconductor systems, correlation has been found to play a minor role in *single-pulse* HHG scenarios by *ab initio* approaches [23–26] and further for disordered [27], topological [28], doped [29], finite [30], and systems with vacancies [31]. Exceptions to this general trend occur in case of enhancement beyond the first plateau where correlation effects may promote specific parts of the HHG spectra, as shown in theoretical works [27,32] and alluded to in experiment [33]. Recently, many-electron correlation effects of HHG have been considered in effective-Hamiltonian models that are strongly correlated under field-free conditions [34–39], such as the Fermi-Hubbard model. In two-dimensional materials [40,41], a decrease in HHG signal is found within a wide range of high-harmonic frequencies as a result of correlational effects. It is found that HHG spectroscopy of correlated materials can uncover ultrafast nonequilibium many-electron dynamics through its dynamical effect on the HHG spectrum.

The question whether one can introduce, control and identify signatures of many-electron correlations by applying external laser pulses to a system that is weakly correlated under field-free conditions seems unexplored so far. It is the purpose of this paper to elucidate this question. If such correlations may be controlled, they provide a pathway for significant enhancement across a wide range of high-harmonic frequencies for band gap materials that are weakly or uncorrelated in their field-free state. In search of utilizing and characterizing such correlational effects during strong-field driving, we enter the finite-sized regime of nanostructured materials. For such nanostructures, even within the independent-electron approach, a significant increase in efficiency can be contributed to quantum confinement [42], and if the system is sufficiently thin, the propagation damping can be reduced [43].

In this paper, we discover methods of laser-inducing strong electron correlation effects in a nanostructured band-gap material by a two-color pump-probe HHG scheme. Furthermore, we characterize the origin of these effects to stem from edge states (ESs) and demonstrate their ability to create a significant enhancement of the HHG yield over a wide spectral range. This paper is organized as follows. In Sec. II, the theoretical model and methods are discussed. In Sec. III, the results are presented, and Sec. IV concludes.

II. THEORETICAL MODEL AND METHODS

We apply a model based on time-dependent density functional theory (TDDFT) [44]. This approach allows us to include contributions from all bands in the band structure and consider dynamical electron-electron interaction. Macroscopic propagation effects are neglected. Our approach is therefore valid for thin target materials, which are feasible experimentally [45–49]. We consider samples with nanoscale precision. Such precision is obtainable in production of, e.g., ZnO nanowires [50]. To make the discussion as general as possible, we consider a nanoscale model sample of a generic band gap material with band gap energy of multiple infrared (IR) photons, as well as its bulk limit. Features of the present findings can thus be expected for a range of

band gap materials if accounting for system-specific rescaling of laser parameters. We work in atomic units with a linear chain of N ions, each with nuclear charge $Z = 4$ generating a static ionic potential, $v_{\rm ion}(x) = -\sum_{i=0}^{N-1} Z[(x - x_i)^2 + \epsilon]^{-1/2}$ for nuclear coordinates $x_i = [i - (N-1)/2]a$, separated by lattice constant $a = 7$. To model the nanoscale system, we consider $N = 80$, which matches the ∼30 nm diameter of ZnO nanorods [50]. We consider a charge and spin neutral system with the three-dimensional (3D) expression for local spin-density exchange and apply a softened Coulomb potential, with the softening parameter $\epsilon = 2.25$, to mimic 3D electrons driven in the linear polarization direction. We have performed extensive scans over system size. The reported findings are consistent in the range of $60 \leqslant N \leqslant 160$. Below $N = 60$, we observe behavior of atomic nature [30]. Above $N = 160$, we observe convergence to the bulk response [26]. The system is ideal for comparisons with previous theoretical works, as it has been studied extensively in the literature [25–31] and is generally considered weakly correlated, as correlations have shown to be negligible in the literature for single-pulse studies, whether being bulk, finite, doped, containing impurities, or topological edges. When applying a laser pulse described by its vector potential $A(t)$, the Kohn-Sham (KS) orbitals $\varphi_{\sigma,i}(x,t)$ are propagated through the time-dependent KS equation $i\partial_t \varphi_{\sigma,i}(x,t) = \{-\partial_x^2/2 - iA(t)\partial_x + \tilde{v}_{\rm KS}[n_\sigma](x,t)\}\varphi_{\sigma,i}(x,t)$ using the time-dependent KS potential

$$\tilde{v}_{\rm KS}[\{n_\sigma\}](x,t) = v_{\rm ion}(x) + v_H[n](x,t) + v_{xc}[\{n_\sigma\}](x,t). \tag{1}$$

The dynamical part hereof consists of the Hartree potential $v_H[n](x,t) = \int dx' n(x',t)[(x-x')^2 + \epsilon]^{-1/2}$, and the exchange-correlation potential, which in the local spin-density approximation is given as $v_{xc}[\{n_\sigma\}](x,t) \simeq -[6n_\sigma(x,t)/\pi]^{1/3}$. The spin density and the total density are given, respectively, as $n_\sigma(x,t) = \sum_{i=0}^{N_\sigma - 1} |\varphi_{\sigma,i}(x,t)|^2$, and $n(x,t) = \sum_{\sigma=\uparrow,\downarrow} n_\sigma(x,t)$, with N_σ being the number of electrons with spin $\sigma = \{\uparrow, \downarrow\}$. We have checked that the conclusions of this paper remain unaffected by using another functional [51]. Similarly, the fundamental physics in terms of ES excitation and ES-induced density variations would not change qualitatively by considering, e.g., a TDDFT + U approach [52]. The orbitals obtained by imaginary time propagation are propagated using the Crank-Nicolson method with a predictor-corrector step applying an absorbing potential [53]. In multiple earlier single-IR-pulse studies [25,27–31], all-electron dynamics were well-described in the independent many-electron band structure picture using a "frozen" calculation, corresponding to setting $\tilde{v}_{\rm KS}[\{n_\sigma\}](x,t) \simeq \tilde{v}_{\rm KS}[\{n_\sigma\}](x,0)$. This is equivalent to a noninteracting electron calculation, where all electrons move independently in a static, effective potential which contains the electron-electron interaction but only for the initial static system. We employ the notation of being correlated if going beyond this frozen approach during the HHG process, see also Refs. [23,38,40]. By including the dynamical electron-electron interaction, the full "dynamical" propagation method can be applied with a time-dependent KS potential $\tilde{v}_{\rm KS}[\{n_\sigma\}](x,t)$, and the approach captures laser-induced electron correlation effects. The HHG spectra

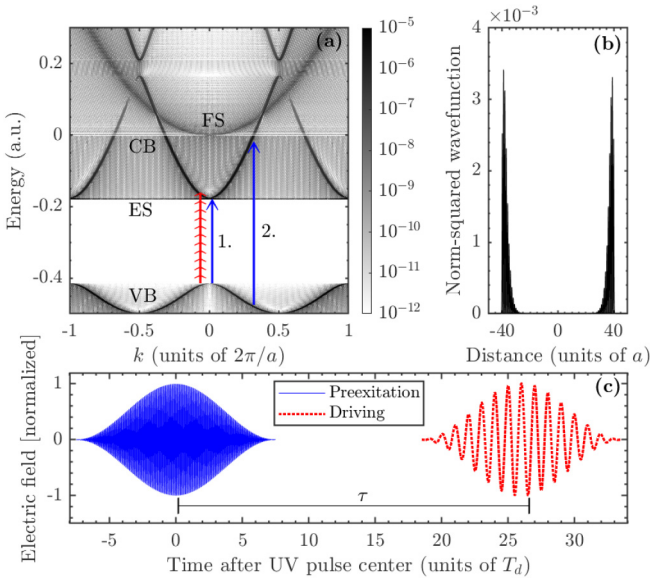

FIG. 1. (a) Band structure with the highest energy valence band (VB) and the lowest energy conduction band (CB). The edge states (ESs) are indicated below the CB by the horizontal line at ≈−0.18. The free-space (FS) dispersion is visible. Arrows denote central photon energies: the smallest red arrows depicting the $11\omega_d$ multiphoton transition, 1. illustrating the pre-excitation pulse when resonant with the ES, and 2. the pre-excitation pulse off-resonant with the ES. (b) The norm-squared wave function in real space of the ES below CB for an $N = 80$ system. (c) Two-color pump-probe pulse sequence with the ultraviolet (UV) pre-excitation pump and the infrared (IR) driving laser pulses in units of the period of the IR laser T_d and with each pulse normalized individually. The pulses drive the transitions in (a), see text for parameters.

are calculated through the modulus squared of the Fourier transformed current. A window function is applied to account for dephasing; it attains the value 1 before the center of the driving pulse, whereafter it follows a $\cos^8$ decay.

III. RESULTS AND DISCUSSION

As a start, we apply imaginary time propagation to obtain the KS orbitals. For large systems, a Fourier transformation of the KS orbitals resolves the band structure [30]. The presence of a band structure shows that the system is only weakly correlated. The band structure consists of two completely filled valence bands (VBs) and numerous unoccupied conduction bands (CBs). In finite-sized systems, several ESs appear, in this model, just below each VB and CB. We examine the interaction with two ESs just below the lowest energy CB [26]. The highest energy VB and lowest energy CB are depicted in Fig. 1(a) for an $N = 80$ system with the ES energy shown by the horizontal line at an energy of ≈−0.18. One of these ESs is depicted in real space in Fig. 1(b). Due to its localization in real space, it is delocalized in momentum space, and all k values within the first Brillouin zone are contained in a single ES. Such ESs have been seen to dominate the electron dynamics in low-dimensional elongated systems such as graphene nanoribbons and carbon nanotubes [54].

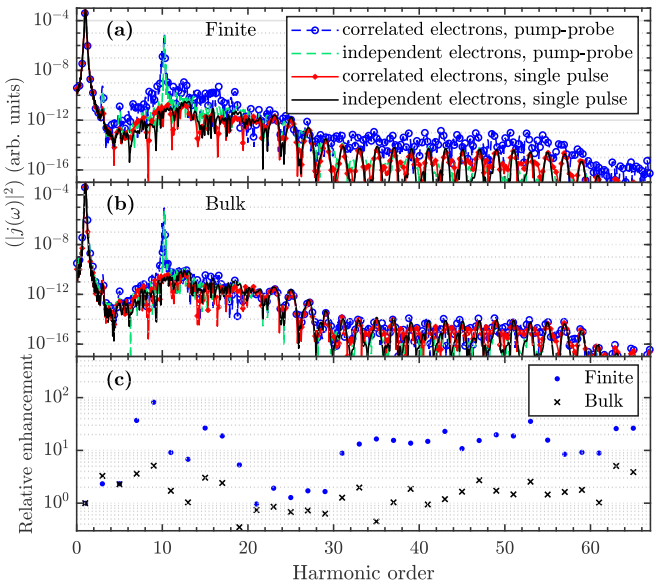

FIG. 2. High-harmonic generation (HHG) spectra (a) for a finite-sized system ($N = 80$) and (b) bulk system for two-color pump-probe and infrared (IR)-only ($n_d = 15$-cycle IR pulse with $\omega_d = 0.023$ and $F_{0,d} = 0.00552$) references in correlated and independent-electron descriptions. (c) Ratio between the pump-probe signal for correlated and independent electrons for $N = 80$ and the bulk system. The 153-cycle ultraviolet (UV) pump with $\omega_p = 0.235$, $F_{0,p} = 0.0005$, and resonant with the edge states (ESs) [see Figs. 1(a) and 1(c)] was at a time $\tau = 26T_d$ earlier than the IR probe.

The two linearly polarized pump-probe pulses of different colors are illustrated in Fig. 1(c). The field can be described by $F(t) = F_p(t) + F_d(t)$, where the subscripts p and d denote a pre-excitation and driving pulse, respectively. Both pulses are sinusoidal waves with a $\sin^2$ envelope function for the vector potential. The 15-cycle IR pulse has a frequency of $\omega_d = 0.023$ ($\lambda_d \simeq 2\mu$m). As seen in Fig. 1(a), an interband process requires at least an 11-photon transfer. The driving field has amplitude $F_{0,d} = 0.00552$ corresponding to an intensity of $\simeq 10^{12}$W/cm^2, as used earlier [25,31]. Applying similar parameters as in earlier two-color pump-probe studies [55], we first consider the pump-probe setting of Fig. 1(c) with two different colored pulses of similar pulse duration and a peak-to-peak delay of $\tau = 26T_d$, which is within the spontaneous decay time of the carriers [55]. Here, $T_d = 2\pi/\omega_d$ is the period of the driving frequency. We apply a 153-cycle pre-excitation pulse tuned either resonantly to the ESs with $\omega_p = 0.235$ or to the CB with $\omega_p = 0.455575$ [Fig. 1(a)]. The pre-excitation pulse allows for controlled population of carriers, which is capable of selectively enhancing specific harmonics within the independent-electron approach [55,56] and not considering ESs. We use the capability of controlled population of carriers to explicitly target multielectron correlation effects to identify the characteristics hereof. To examine nanoscale-related behavior, we populate the ESs of the system with a pre-excitation pulse [see Fig. 1(a), 1. arrow] and find a significant enhancement when including electron correlation. This is shown in Fig. 2, where the parameters are given in the caption. When comparing the single IR pulse reference with the two-color pump-probe result, we see the characteristics of the one-photon resonant transition from the VB to the ES, visible as a peak $\omega \sim 10.2\omega_d$, corresponding to the frequency of the pump pulse ω_p. We have verified by a calculation applying only the pre-excitation pulse, that this peak occurs as a perturbative response. For the finite system, a correlational enhancement appears when comparing the independent-electron and the correlated dynamical methods. For the bulk system, no such correlation effects appear, solidifying the finite-sized characteristic of this effect. The bulk response is found by an $N = 300$ calculation, in which the spectrum has converged to the spectra of a periodic system [26].

The origin of this correlational enhancement relies on the controlled population of the ESs excited by the pump pulse. During the UV pump, these states will fluctuate slightly in energy below the CB, as their energies depend on the time-dependent density distribution. Furthermore, as the ESs are localized in real space and delocalized in momentum space, transitions hereto are allowed from every state in the VB and thereby at a wide range of frequencies. A pre-excitation frequency scan clearly reveals the importance of including correlations to describe finite-sized enhancement, when the UV frequency is in the range of the ESs. As is seen by Fig. 2(c), the correlation enhancement is present at a wide range of harmonic frequencies, including the first plateau, thus entering the range of most current experimental detection. By varying the intensity of the UV pre-excitation pulse, no enhancement at UV intensities $< 10^9$ W/cm^2 is found. For higher intensities, the enhancement persists, and the spectra show a saturationlike convergence at intensities $> 8.8 \times 10^{10}$ W/cm^2. This scaling is especially interesting, as the effect of a band gap pre-excitation was shown to give a reduction of HHG when increasing pre-excitation intensity for uncorrelated bulk ZnO in Ref. [57].

To show that the correlation effect arrives as a result of resonant control of population transfer to the ESs, as compared with a similar controlled carrier population of the band gap a nonresonant pump-probe calculation with a frequency of $\omega_p = 0.455575$ was made [see Fig. 1(a), 2. arrow]. Applying this UV frequency, there are no resonant transitions available to the ES within the spectral range of the pump pulse. The resulting spectra in Fig. 3 show no finite-sized correlational enhancement, as the finite-system response coincides relatively well with the bulk response. The characteristics of the one-photon resonant transition from the VB to the CB is visible as a peak at $\omega \sim 19.8\omega_d$, corresponding to the frequency of the pre-excitation pulse ω_p. This paper indicates that a two-color pump-probe scheme can promote finite-sized effects and increases the limit for bulk-dominated dynamics from $N \sim 60$ ($\sim$22 nm for the present lattice constant) seen in Ref. [30] to $N \sim 220$ ($\sim$81 nm), even more than for converged one-pulse results [26], further elucidating the range of sizes where the ESs affect the electronic behavior [54].

The underlying ultrafast dynamics which provide correlational enhancement can be interpreted as additional correlational excitations, see, e.g., the hauling up effect of Ref. [32]. In the present case, a time-resolved investigation is useful. This is done with the correlated propagation method applying various peak-to-peak pump-probe delays τ [Fig 1(c)]. To resolve the dynamics in time, a 2-cycle driving IR pulse with a vanishing carrier envelope phase was applied.

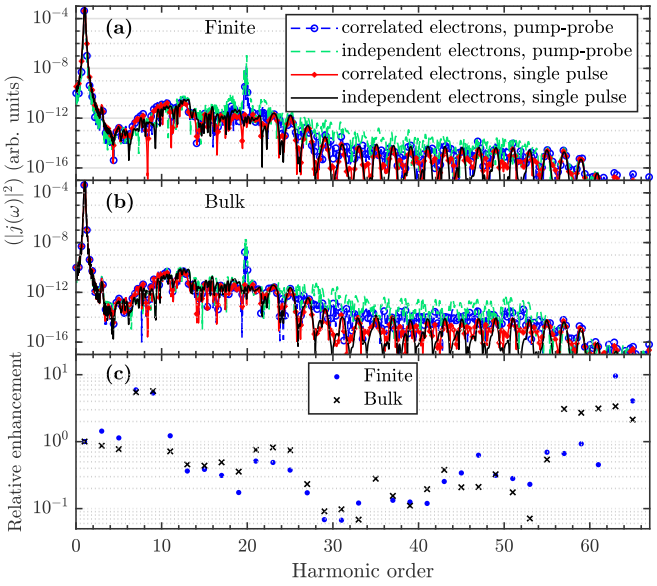

FIG. 3. As Fig. 2, but for $\omega_p = 0.455575$, off resonant with the edge states (ESs) [see Fig. 1(a)].

The resulting spectra are depicted in Fig. 4(a) as a function of τ with certain lineouts depicted in Fig. 4(c). By comparing the HHG spectra at different τ, see, e.g., $\tau = 21T_d$ and $\tau = 26T_d$ in Fig. 4(c), it shows that if including laser-induced correlation, the HHG spectra depends strongly on τ and hence on the electron dynamics in the nanoscale material after the pre-excitation pulse. A direct way of gaining insight into the underlying dynamics is by considering the time-dependent density of a pre-excited system as in Fig. 4(b). By resonant coupling of the ESs, the edge of the system is populated during the pre-excitation pulse. Soon hereafter, the populated localized ESs will create an increased repulsion, resulting in an electron wave propagating from the edges inward toward the center of the sample. The dynamical ES-induced electron-density fluctuation propagates and interferes throughout the system [Fig. 4(b)]. This fluctuation of electron density leads to a time-dependent change in the KS potential, which breaks the translational symmetry within the sample. The density fluctuates even though nothing is driving the system after the pre-excitation pulse has ended at $7.5T_d$. The Hartree term of the dynamical KS potential drives the system away from regions where the interfering density fluctuation is localized. Consequently, when applying a driving pulse, its interaction with the time-dependent electron density will be τ dependent and result in τ dependent spectra. Such correlation effects were revealed in Fig. 2 to contribute to an important effect when applying a driving field to a pre-excited nanoscale system. One can observe in Fig. 4 that the timescale of the density fluctuations are like that of the fluctuations in the HHG spectra. We note that modeling of the two-color pump-probe scheme of Fig. 4 by an independent-electron simulation (with frozen KS potential) will show no variation of the density as a function of τ after the end of the pre-excitation pulse, as no repulsion is initialized in the ESs. For such a calculation, a slight τ dependency can still be witnessed in the HHG spectra since the wave packet initialized by the pre-excitation pump pulse is probed at different times by the driving pulse

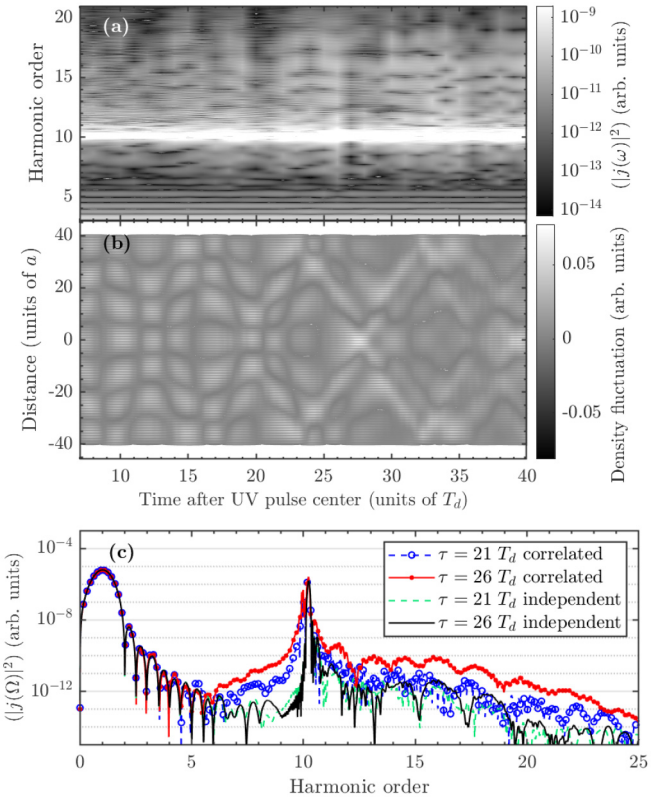

FIG. 4. (a) High-harmonic generation (HHG) spectra of a finite ($N = 80$) system as a function of time-delay between pre-excitation by an $n_p = 153$-cycle ultraviolet (UV) pulse with $\omega_p = 0.235$ and $F_{0,p} = 0.0005$ and a $n_d = 2$-cycle infrared (IR) pulse with $\omega_d = 0.023$ and $F_{0,d} = 0.00552$ driving pulse, applying correlated dynamical propagation. (b) The density fluctuations $n(x, t) - n(x, 0)$ of the system applying the correlated dynamical method given as a function of time, with parameters of (a) but with no driving field. (c) HHG spectra at certain τ from (a) compared with spectra from calculations in the same setting but with an independent-electron approach.

[Fig. 4(c)]. This τ dependency will, however, in a full simulation be completely overshadowed by the large laser-induced correlation effects, as seen when comparing spectra resulting from the independent and correlated calculations [Fig. 4(c)]. This difference in the pump-probe-delay behavior of the spectra with the independent-electron and correlated approaches indicates that, if a significant time-dependent fluctuation is observed in the HHG spectra, it can be a signature of an underlying correlational dynamic, which further alludes to a possibility for two-color pump-probe HHG spectroscopy to provide a pathway to resolve such coherent many-electron dynamics in finite systems. We have found that this delay-dependency is also present for the 15-cycle driving field of Fig. 2, even though the timescale of the fluctuations cannot be resolved. This indicates that by tuning τ of a pump-probe HHG scheme, one can experimentally test for indications of dynamics beyond independent-electron approaches. The calculations furthermore suggest that the ability to tune τ is crucial for achieving optimal correlational enhancement. The results for large temporal overlap of the UV pre-excitation pump pulse and the IR driving pulses (not shown) show lack of correlational enhancement, as do the previous one-pulse

studies [25,26,29–31]. Thus, the correlations need time to initiate a detectable change in the HHG signal.

IV. CONCLUSIONS

In conclusion, the present results elucidate the importance of considering laser-induced electron correlation effects when investigating HHG in nanosized band gap materials in pump-probe schemes. We characterized the correlational enhancement as a consequence of ES-induced electron fluctuations and showed that these many-electron dynamics enforce a significant time dependency in the HHG spectra when considered as a function of the time delay between the pump and the probe pulse. The sensitivity to the time delay is much larger when laser-induced electron correlations are accounted for than when they are not, as in the independent-electron approach. This difference in the behavior of the spectra indicates that the underlying dynamics might be revealed through HHG spectroscopy or harnessed for optimization of the enhancement in two-color pump-probe HHG. As the localized ESs initialize the dynamics, it would be interesting to investigate in the future if similar effects can stem from localized atomlike orbitals introduced by, e.g., doping.

ACKNOWLEDGMENTS

This paper was supported by the Danish Council for Independent Research (Grant No. 9040-00001B).

[1] S. Ghimire, A. D. DiChiara, E. Sistrunk, P. Agostini, L. F. DiMauro, and D. A. Reis, Observation of high-order harmonic generation in a bulk crystal, Nat. Phys. **7**, 138 (2011).

[2] O. Schubert, M. Hohenleutner, F. Langer, B. Urbanek, C. Lange, U. Huttner, D. Golde, T. Meier, M. Kira, S. W. Koch, and R. Huber, Sub-cycle control of terahertz high-harmonic generation by dynamical Bloch oscillations, Nat. Photonics **8**, 119 (2014).

[3] T. T. Luu, M. Garg, S. Yu. Kruchinin, A. Moulet, M. Th. Hassan, and E. Goulielmakis, Extreme ultraviolet high-harmonic spectroscopy of solids, Nature (London) **521**, 498 (2015).

[4] M. Garg, H. Y. Kim, and E. Goulielmakis, Ultimate waveform reproducibility of extreme-ultraviolet pulses by high-harmonic generation in quartz, Nat. Photonics **12**, 291 (2018).

[5] S. Yu. Kruchinin, F. Krausz, and V. S. Yakovlev, Colloquium: Strong-field phenomena in periodic systems, Rev. Mod. Phys. **90**, 021002 (2018).

[6] T. Tamaya, A. Ishikawa, T. Ogawa, and K. Tanaka, Diabatic Mechanisms of Higher-Order Harmonic Generation in Solid-State Materials under High-Intensity Electric Fields, Phys. Rev. Lett. **116**, 016601 (2016).

[7] L. Yue and M. B. Gaarde, Imperfect Recollisions in High-Harmonic Generation in Solids, Phys. Rev. Lett. **124**, 153204 (2020).

[8] L. Yue and M. B. Gaarde, Structure gauges and laser gauges for the semiconductor Bloch equations in high-order harmonic generation in solids, Phys. Rev. A **101**, 053411 (2020).

[9] H. Lakhotia, H. Y. Kim, M. Zhan, S. Hu, S. Meng, and E. Goulielmakis, Laser picoscopy of valence electrons in solids, Nature (London) **583**, 55 (2020).

[10] S. Ghimire, A. D. DiChiara, E. Sistrunk, G. Ndabashimiye, U. B. Szafruga, A. Mohammad, P. Agostini, L. F. DiMauro, and D. A. Reis, Generation and propagation of high-order harmonics in crystals, Phys. Rev. A **85**, 043836 (2012).

[11] P. G. Hawkins, M. Yu. Ivanov, and V. S. Yakovlev, Effect of multiple conduction bands on high-harmonic emission from dielectrics, Phys. Rev. A **91**, 013405 (2015).

[12] M. Hohenleutner, F. Langer, O. Schubert, M. Knorr, U. Huttner, S. W. Koch, M. Kira, and R. Huber, Real-time observation of interfering crystal electrons in high-harmonic generation, Nature (London) **523**, 572 (2015).

[13] M. Wu, D. A. Browne, K. J. Schafer, and M. B. Gaarde, Multilevel perspective on high-order harmonic generation in solids, Phys. Rev. A **94**, 063403 (2016).

[14] Y. S. You, D. A. Reis, and S. Ghimire, Anisotropic high-harmonic generation in bulk crystals, Nat. Phys. **13**, 345 (2017).

[15] L. Li, P. Lan, X. Zhu, T. Huang, Q. Zhang, M. Lein, and P. Lu, Reciprocal-Space-Trajectory Perspective on High-Harmonic Generation in Solids, Phys. Rev. Lett. **122**, 193901 (2019).

[16] T. Ikemachi, Y. Shinohara, T. Sato, J. Yumoto, M. Kuwata-Gonokami, and K. L. Ishikawa, Trajectory analysis of high-order-harmonic generation from periodic crystals, Phys. Rev. A **95**, 043416 (2017).

[17] T. Higuchi, M. I. Stockman, and P. Hommelhoff, Strong-Field Perspective on High-Harmonic Radiation from Bulk Solids, Phys. Rev. Lett. **113**, 213901 (2014).

[18] G. Vampa, C. R. McDonald, G. Orlando, D. D. Klug, P. B. Corkum, and T. Brabec, Theoretical Analysis of High-Harmonic Generation in Solids, Phys. Rev. Lett. **113**, 073901 (2014).

[19] K. C. Kulander, K. J. Schafer, and J. L. Krause, Dynamics of short-pulse excitation, ionization and harmonic conversion, in *Super-Intense Laser-Atom Physics*, edited by B. Piraux, A. L'Huillier, and K. Rzaążewski (Springer US, Boston, 1993), pp. 95–110.

[20] P. B. Corkum, Plasma Perspective on Strong Field Multiphoton Ionization, Phys. Rev. Lett. **71**, 1994 (1993).

[21] M. Lewenstein, Ph. Balcou, M. Y. Ivanov, A. L'Huillier, and P. B. Corkum, Theory of high-harmonic generation by low-frequency laser fields, Phys. Rev. A **49**, 2117 (1994).

[22] G. Vampa, T. J. Hammond, N. Thiré, B. E. Schmidt, F. Légaré, C. R. McDonald, T. Brabec, D. D. Klug, and P. B. Corkum, All-Optical Reconstruction of Crystal Band Structure, Phys. Rev. Lett. **115**, 193603 (2015).

[23] N. Tancogne-Dejean, O. D. Mücke, F. X. Kärtner, and A. Rubio, Impact of the Electronic Band Structure in High-Harmonic Generation Spectra of Solids, Phys. Rev. Lett. **118**, 087403 (2017).

[24] N. Tancogne-Dejean, O. D. Mücke, F. X. Kärtner, and A. Rubio, Ellipticity dependence of high-harmonic generation in solids originating from coupled intraband and interband dynamics, Nat. Commun. **8**, 745 (2017).

[25] K. K. Hansen, T. Deffge, and D. Bauer, High-order harmonic generation in solid slabs beyond the single-active-electron approximation, Phys. Rev. A **96**, 053418 (2017).
[26] C. Yu, H. Iravani, and L. B. Madsen, Crystal-momentum-resolved contributions to multiple plateaus of high-order harmonic generation from band-gap materials, Phys. Rev. A **102**, 033105 (2020).
[27] C. Yu, K. K. Hansen, and L. B. Madsen, High-order harmonic generation in imperfect crystals, Phys. Rev. A **99**, 063408 (2019).
[28] D. Bauer and K. K. Hansen, High-Harmonic Generation in Solids with and without Topological Edge States, Phys. Rev. Lett. **120**, 177401 (2018).
[29] C. Yu, K. K. Hansen, and L. B. Madsen, Enhanced high-order harmonic generation in donor-doped band-gap materials, Phys. Rev. A **99**, 013435 (2019).
[30] K. K. Hansen, D. Bauer, and L. B. Madsen, Finite-system effects on high-order harmonic generation: From atoms to solids, Phys. Rev. A **97**, 043424 (2018).
[31] H. Iravani, K. K. Hansen, and L. B. Madsen, Effects of vacancies on high-order harmonic generation in a linear chain with band gap, Phys. Rev. Research **2**, 013204 (2020).
[32] T. Ikemachi, Y. Shinohara, T. Sato, J. Yumoto, M. Kuwata-Gonokami, and K. L. Ishikawa, Time-dependent Hartree-Fock study of electron-hole interaction effects on high-order harmonic generation from periodic crystals, Phys. Rev. A **98**, 023415 (2018).
[33] G. Ndabashimiye, S. Ghimire, M. Wu, D. A. Browne, K. J. Schafer, M. B. Gaarde, and D. A. Reis, Solid-state harmonics beyond the atomic limit, Nature (London) **534**, 520 (2016).
[34] S. Imai, A. Ono, and S. Ishihara, High Harmonic Generation in a Correlated Electron System, Phys. Rev. Lett. **124**, 157404 (2020).
[35] Y. Murakami, M. Eckstein, and P. Werner, High-Harmonic Generation in Mott Insulators, Phys. Rev. Lett. **121**, 057405 (2018).
[36] R. E. F. Silva, I. V. Blinov, A. N. Rubtsov, O. Smirnova, and M. Ivanov, High-harmonic spectroscopy of ultrafast many-body dynamics in strongly correlated systems, Nat. Photonics **12**, 266 (2018).
[37] S. Takayoshi, Y. Murakami, and P. Werner, High-harmonic generation in quantum spin systems, Phys. Rev. B **99**, 184303 (2019).
[38] N. Tancogne-Dejean, M. A. Sentef, and A. Rubio, Ultrafast Modification of Hubbard U in a Strongly Correlated Material: *Ab Initio* High-Harmonic Generation in NiO, Phys. Rev. Lett. **121**, 097402 (2018).
[39] M. Lysne, Y. Murakami, M. Schüler, and P. Werner, High-harmonic generation in spin-orbit coupled systems, Phys. Rev. B **102**, 081121(R) (2020).
[40] N. Tancogne-Dejean and A. Rubio, Atomic-like high-harmonic generation from two-dimensional materials, Sci. Adv. **4**, eaao5207 (2018).
[41] G. Le Breton, A. Rubio, and N. Tancogne-Dejean, High-harmonic generation from few-layer hexagonal boron nitride: Evolution from monolayer to bulk response, Phys. Rev. B **98**, 165308 (2018).
[42] C. R. McDonald, K. S. Amin, S. Aalmalki, and T. Brabec, Enhancing High Harmonic Output in Solids through Quantum Confinement, Phys. Rev. Lett. **119**, 183902 (2017).
[43] I. Kilen, M. Kolesik, J. Hader, J. V. Moloney, U. Huttner, M. K. Hagen, and S. W. Koch, Propagation Induced Dephasing in Semiconductor High-Harmonic Generation, Phys. Rev. Lett. **125**, 083901 (2020).
[44] E. Runge and E. K. U. Gross, Density-Functional Theory for Time-Dependent Systems, Phys. Rev. Lett. **52**, 997 (1984).
[45] H. Liu, Y. Li, Y. S. You, S. Ghimire, T. F. Heinz, and D. A. Reis, High-harmonic generation from an atomically thin semiconductor, Nat. Phys. **13**, 262 (2017).
[46] M. Garg, M. Zhan, T. T. Luu, H. Lakhotia, T. Klostermann, A. Guggenmos, and E. Goulielmakis, Multi-petahertz electronic metrology, Nature (London) **538**, 359 (2016).
[47] S. Nakamura, K. Katsumi, H. Terai, and R. Shimano, Nonreciprocal Terahertz Second-Harmonic Generation in Superconducting NbN under Supercurrent Injection, Phys. Rev. Lett. **125**, 097004 (2020).
[48] M. Taucer, T. J. Hammond, P. B. Corkum, G. Vampa, C. Couture, N. Thiré, B. E. Schmidt, F. Légaré, H. Selvi, N. Unsuree, B. Hamilton, T. J. Echtermeyer, and M. A. Denecke, Nonperturbative harmonic generation in graphene from intense midinfrared pulsed light, Phys. Rev. B **96**, 195420 (2017).
[49] N. Yoshikawa, T. Tamaya, and K. Tanaka, High-harmonic generation in graphene enhanced by elliptically polarized light excitation, Science **356**, 736 (2017).
[50] G. Grinblat, M. Rahmani, E. Cortés, M. Caldarola, D. Comedi, S. A. Maier, and A. V. Bragas, High-efficiency second harmonic generation from a single hybrid Zno nanowire/Au plasmonic nano-oligomer, Nano Lett. **14**, 6660 (2014).
[51] J. P. Perdew, K. Burke, and M. Ernzerhof, Generalized Gradient Approximation Made Simple, Phys. Rev. Lett. **77**, 3865 (1996).
[52] N. Tancogne-Dejean, M. J. T. Oliveira, and A. Rubio, Self-consistent DFT $+U$ method for real-space time-dependent density functional theory calculations, Phys. Rev. B **96**, 245133 (2017).
[53] D. Bauer, H. Bauke, T. Brabec, T. Fennel, C. R. McDonald, D. B. Milošević, S. Pabst, C. Peltz, G. Pöplau, R. Santra, and C. Varin, *Computational Strong-Field Quantum Dynamics* (De Gruyter, Berlin, 2017).
[54] O. Hod, J. E. Peralta, and G. E. Scuseria, Edge effects in finite elongated graphene nanoribbons, Phys. Rev. B **76**, 233401 (2007).
[55] L.-J. Lü and X.-B. Bian, Multielectron interference of intraband harmonics in solids, Phys. Rev. B **100**, 214312 (2019).
[56] X. Song, S. Yang, R. Zuo, T. Meier, and W. Yang, Enhanced high-order harmonic generation in semiconductors by excitation with multicolor pulses, Phys. Rev. A **101**, 033410 (2020).
[57] Z. Wang, H. Park, Yu. H. Lai, J. Xu, C. I. Blaga, F. Yang, P. Agostini, and L. F. DiMauro, The roles of photo-carrier doping and driving wavelength in high harmonic generation from a semiconductor, Nat. Commun. **8**, 1686 (2017).